Progress Report: DEFG0204ER46122

Final Report

Structural Investigations of Complex Oxides Using Synchrotron Radiation

PI - H. zur Loye
Department of Chemistry and Biochemistry
University of South Carolina

This project focused on the synthesis of novel oxide materials and their characterization using synchrotron radiation in collaboration with Dr. Tom Vogt at Brookhaven National Laboratory, National Synchrotron Light Source and by single crystal X-ray diffraction. We have synthesized many new oxides compositions and have structurally characterized these materials.

Brief summary of personnel.

During the three years several individuals worked on this project and were supported to different degrees by the funds available. Two postdocs, Dr. Michael Lufaso and Dr. Rene Macquart, worked on the synthesis and crystal growth. Two graduate students, Samuel Mugavero and Dr. William Gemmill, were also involved in this project. The papers that resulted from this work are listed at the end of this report.

During the final year of this grant we completed the characterization of several compounds and begun the exploration of others. For example, the synthesis of *$LnNaIrO_4$ (Ln = Gd-Er, Y)* was reported in the last report. At that time we were still working on the magnetic property measurements. At this point, a paper has been submitted and is currently in press in Solid State Sciences. In this work, single crystals of $Gd_{0.96}Na_{1.04}IrO_4$, $Tb_{0.93}Na_{1.07}IrO_4$, $Dy_{0.94}Na_{1.06}IrO_4$, $Ho_{0.90}Na_{1.10}IrO_4$, $Er_{0.75}Na_{1.25}IrO_4$, and $Y_{0.92}Na_{1.08}IrO_4$, were grown out of an acidic molten NaOH/CsOH flux. Typically, the hydroxide starting reagents contained about 15% water by weight. Crystals were grown in silver tubes that had been previously flame sealed at one end. The tops of the tubes were crimped, and folded three times before being placed upright into a programmable box furnace. The tubes were heated to 700°C in one hour, held at that temperature for 24 h and then cooled to room temperature by shutting off the furnace. The black, rod-shaped crystals were removed from the flux matrix by dissolving the flux in deionized water aided by sonication. Attempts were made to synthesize these compositions by traditional solid state powder techniques, but were unsuccessful because inevitably the $Ln_2Ir_2O_7$ pyrochlore phases formed under the reaction conditions used. The magnetic susceptibilities of loose single crystals of $Gd_{0.96}Na_{1.04}IrO_4$, $Tb_{0.93}Na_{1.07}IrO_4$, $Dy_{0.94}Na_{1.06}IrO_4$, $Ho_{0.90}Na_{1.10}IrO_4$, $Er_{0.75}Na_{1.25}IrO_4$, and $Y_{0.92}Na_{1.08}IrO_4$, were measured using a Quantum Design MPMS XL SQUID magnetometer. The samples were measured under both zero field cooled (ZFC) and field cooled (FC) conditions in applied fields of 1 and 10 kG over the temperature range of $2\ K \leq T \leq 300\ K$. The samples were contained in gel capsules suspended in a plastic straw for immersion into the SQUID.

The structure of these oxides features rutile-like chains of edge sharing IrO_6 octahedra that corner share to columns of NaO_6 trigonal prisms. The layer containing the iridium cations is shown below.

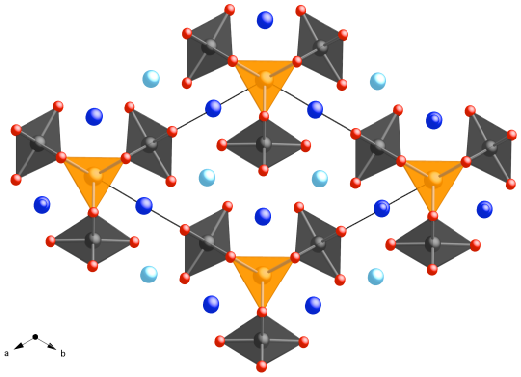

Figure 1. *Structure of $LnNaIrO_6$ highlighting the black IrO_6 octahedra and orange NaO_6 trigonal prisms. The rare earths are shown in blue.*

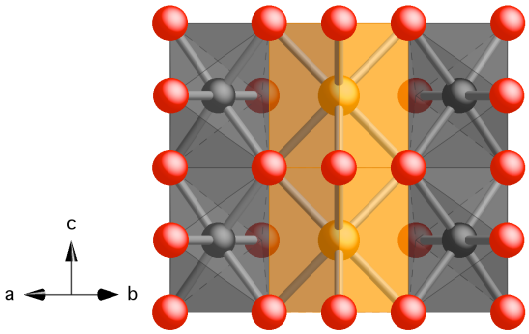

Figure 2. *Infinite chains of face-sharing NaO_6 trigonal prism share edges with infinite chains of edge-sharing IrO_6 octahedra.*

Single crystals of $Ln_{1-x}Na_{1+x}IrO_4$ were grown out of a mixed sodium/cesium hydroxide flux and crystallize in the hexagonal space group *P*-62*m* with lattice parameters ranging from a = 9.3872(2) to 9.4596(3) Å and c = 3.1512(1) to 3.2030(2) Å. These compounds are structurally related to the $Ca_{2-x}IrO_4$ family of iridates that was first reported many years ago. Ideally, $Ca_{2-x}IrO_4$ would have the generic formula A_2BO_4, where *A* is a large electropositive cation, such as an alkali or alkaline earth metal, and *B* represents a smaller transition metal. The ideal composition for the series reported by us, $Ln_{1-x}Na_{1+x}IrO_4$ (*Ln* = Gd – Er, Y; x = 0.04-0.25) would be $LnNaIrO_4$, leading to the generic formula, $AA'BO_4$. The charge on the *A*-site in both ideal structures is +4, but is maintained in the $LnNaIrO_4$ structure by a lanthanide and sodium cation (3 + 1) in place of the two calcium cations (2 + 2) in $Ca_{2-x}IrO_4$. One sodium cation in $Ln_{1-x}Na_{1+x}IrO_4$ (*Ln* = Gd – Er, Y; x = 0.04-0.25) occupies the trigonal prismatic 1*a*-site located at the corner of the unit cell, which is empty in the cation deficient $Ca_{2-x}IrO_4$ (~ $Ca_5Ir_3O_{12}$). A polyhedral representation of the $Ln_{1-x}Na_{1+x}IrO_4$ (*Ln* = Gd – Er, Y; x = 0.04-0.25) crystal structure is shown in Figures 1 and 2. The structure consists of a network of edge-shared and face-shared polyhedra extending infinitely in the *z*-direction with the NaO_6 trigonal prisms anchoring three IrO_6 octahedra at the corners of the unit cell. The unit cell can be subdivided into two alternating layers, with the first, $NaIr_3O_6$, containing only iridium and sodium atoms and the other, $(Na_4Ln_2)Ln_4O_{12}$ composed of only sodium and the respective lanthanide. The first layer repeats to complete the unit cell and creates a face-shared arrangement of NaO_6 trigonal prisms that in turn edge-share with the chains of edge-sharing IrO_6 octahedra extending infinitely in the *z*-direction. The NaO_6 trigonal prisms additionally face-share with the $Ln(2)/Na(2)O_7$ capped, trigonal prisms that themselves edge-share with each other and face-share with LnO_9 distorted, tri-capped trigonal prisms.

The lanthanide content in the $Ln_{1-x}Na_{1+x}IrO_4$ (*Ln* = Gd – Er; x = 0.04 – 0.25) series decreases as the size of the lanthanide metal decreases. To compensate for the decrease in lanthanide content, the amount of sodium increases proportionally, which necessitates an increase in the oxidation state of the iridium to maintain charge balance. The increase in the oxidation state of iridium is reflected in the shortening of the Ir-O bond distances in the IrO_6 octahedra. A plot of the Ir-O(1), Ir-O(2), and Ir-O(3) bond distances as a function of iridium oxidation state is shown in Fig. 3. The composition with the largest lanthanide and the largest

rare earth content in this series, $Gd_{0.96}Na_{1.04}IrO_4$, has the lowest oxidation state of iridium, +4.08 and, hence, the longest Ir-O bond lengths, while $Er_{0.75}Na_{1.25}IrO_4$, containing the smallest lanthanide and the smallest rare earth content in this series, has the highest oxidation state of iridium, +4.50, and hence, the shortest Ir-O bond lengths.

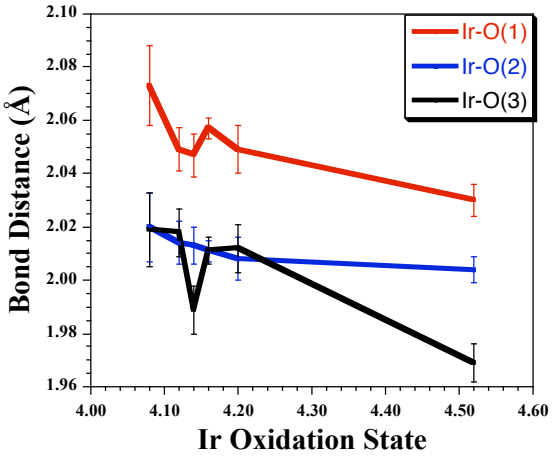

Figure 3. *Plot of the Ir-O bond distances as a function of the iridium oxidation state.*

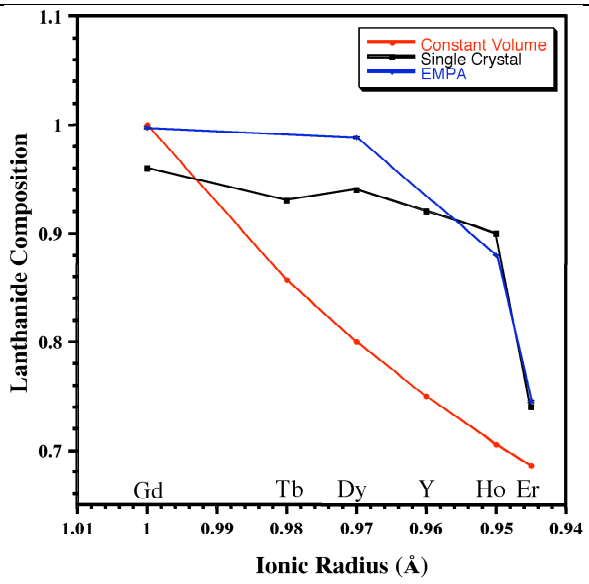

Figure 4. *Plot of lanthanide content as a function of lanthanide size as determined from single crystal X-ray diffraction (black), electron microprobe analysis (blue), and as calculated using a constant volume assumption (red).*

Electron Microprobe Analysis (EMPA) measurements were performed to confirm the compositions obtained from the single crystal X-ray diffraction analysis. While it was not possible to obtain data for all compositions, the trend in the collected data support the numbers obtained from the diffraction analysis. To determine if these compositions are reasonable, a theoretical composition for each compound was calculated based on a constant volume assumption. In these calculation, the composition with the largest lanthanide in the series, $Gd_{0.96}Na_{1.04}IrO_4$, was arbitrarily set to have a combined *Ln* + Na volume of 1.0 (arbitrary units) and was used as the reference point for the calculations. As the lanthanum cation size decreased, the required decrease in the *Ln*:Na ratio to keep the summed volume constant was determined for each lanthanide in the series. The results are shown in Fig. 4 which shows a plot of the lanthanide content based on crystallographic data, on the EMPA measurements, and on the constant volume calculated values, as a function of the lanthanide ionic radius. The general trend in each of the data and the magnitudes of the data are consistent: as the size of the lanthanide decreases the lanthanide content decreases concomitantly.

Magnetism

The temperature dependencies of the magnetic susceptibility data for $Ln_{1-x}Na_{1+x}IrO_4$ (*Ln* = Gd – Er; x = 1.04 – 1.25) at 10 kG are shown in Fig. 5. The magnetic susceptibility data for

$Y_{0.92}Na_{1.08}IrO_4$ is shown in Fig. 6 for scale reasons. The FC and ZFC data overlay in all cases over the temperature range investigated and, hence, only the ZFC data is shown.

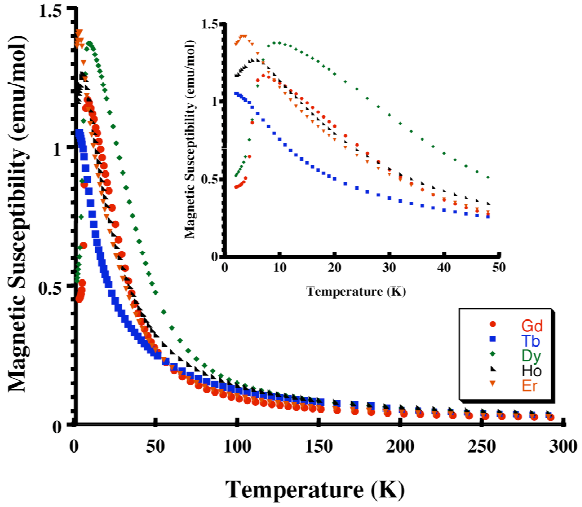

Figure 5. *Plot of the zero field cooled magnetic susceptibility of $Gd_{0.96}Na_{1.04}IrO_4$ (red), $Tb_{0.93}Na_{1.07}IrO_4$ (blue), $Dy_{0.94}Na_{1.06}IrO_4$ (green), $Ho_{0.90}Na_{1.10}IrO_4$ (black), and $Er_{0.75}Na_{1.25}IrO_4$ (orange). The low temperature region is expanded in the inset.*

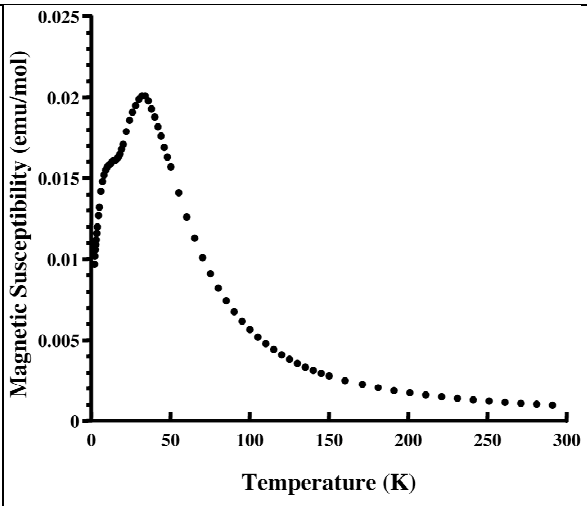

Figure 6. *Plot of the zero field cooled magnetic susceptibility of $Y_{0.92}Na_{1.08}IrO_4$.*

Fitting the inverse susceptibility data from 100 – 300 K, the effective magnetic moments for $Gd_{0.96}Na_{1.04}IrO_4$, $Tb_{0.93}Na_{1.07}IrO_4$, $Dy_{0.94}Na_{1.06}IrO_4$, $Ho_{0.90}Na_{1.10}IrO_4$, $Er_{0.75}Na_{1.25}IrO_4$, and $Y_{0.92}Na_{1.08}IrO_4$ were calculated and are listed along with the theoretical magnetic moments in Table 1.

$Ln_{1-x}Na_{1+x}IrO_4$	μ_{eff}	μ_{cal}
$Gd_{0.96}Na_{1.04}IrO_4$	7.80	7.78
$Tb_{0.93}Na_{1.07}IrO_4$	9.90	9.16
$Dy_{0.94}Na_{1.06}IrO_4$	9.90	10.11
$Ho_{0.90}Na_{1.10}IrO_4$	10.50	9.64
$Er_{0.75}Na_{1.25}IrO_4$	8.87	7.24
$Y_{0.92}Na_{1.08}IrO_4$	1.29	1.45

These effective magnetic moments include contributions from the lanthanide cation and the iridium (IV) cation, except in the case of $Y_{0.92}Na_{1.08}IrO_4$ where iridium is the only magnetic cation. Note: in determining the theoretical moment, no contribution from any Ir^{+5}, which has a non-magnetic ground state, was included. The agreement between the measured and calculated magnetic moments, which are mostly dominated by the contribution from the lanthanide cation, is good. The Ir^{4+} (d^5) cation is spin ½ and magnetic interactions between the edge-shared IrO_6 octahedra along the *c*-axis can reasonably be expected. $Gd_{0.96}Na_{1.04}IrO_4$, $Dy_{0.94}Na_{1.06}IrO_4$, $Ho_{0.90}Na_{1.10}IrO_4$, and $Er_{0.75}Na_{1.25}IrO_4$ exhibit antiferromagnetic correlations below 15 K, Fig. 5, whereas in the case of $Tb_{0.93}Na_{1.07}IrO_4$, magnetic correlations do not appear to occur until below 2

K. The magnetic susceptibility data of $Y_{0.92}Na_{1.08}IrO_4$, Fig. 6, exhibit the highest magnetic transition temperature of 33 K, with a second magnetic transition around 10 K, due to magnetic interactions between the iridium cations in the chains of edge sharing IrO_6 octahedra.

(Ln$_2$Na)NaPtO$_6$ Ln = La, Nd; (Ln$_{2.5}$Na$_{0.5}$)NaRhO$_6$ (Ln = La, Pr, Nd)

In the previous report we mentioned the preparation of *(Ln$_2$Na)NaPtO$_6$ Ln = La, Nd; (Ln$_{2.5}$Na$_{0.5}$)NaRhO$_6$ (Ln = La, Pr, Nd)*. This work has now been published and represents a continuation of our research on 2H-perovskite related oxides where we only recently succeeded in a) incorporating a lanthanide cation on the A-site and b) having mixed metal occupancy on the A-site. These 5 compounds are the only examples to date that exhibit these two characteristics. The structure for $(Nd_{2.5}Na_{0.5})NaRhO_6$, containing sodium in a trigonal prismatic coordination environment, is shown below and is representative of the other compositions.

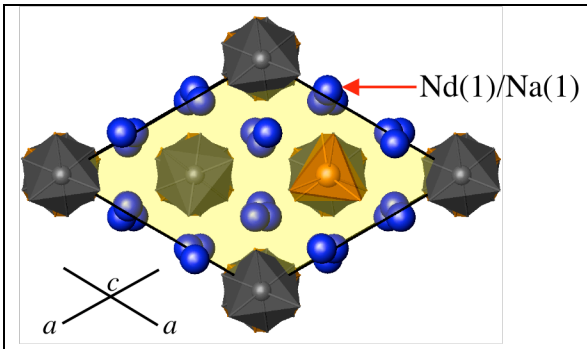

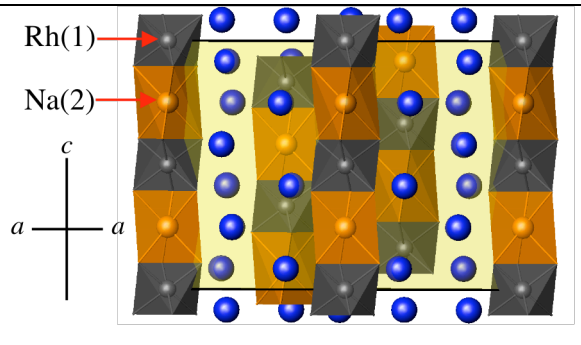

Figure 7. *The lanthanide/sodium is in an 8-coordinate environment. Rhodium is in octahedral coordination and sodium is in trigonal prismatic coordination.*

The standard cubic perovskite has formula ABO_3 and can be thought of as a network of corner sharing octahedra with the *A* cations occupying the cubo-octahedral cavities between the octahedra. Changes in the oxygen packing of the cubic structure leads to the hexagonal perovskite structure. In terms of layer stacking the standard cubic perovskite is composed of $[AO_3]$ layers with ABC stacking with the *B* cations filling the thus formed octahedral sites. The hexagonal system (2H perovskite) is composed of $[AO_3]$ layers stacked in an AB fashion with the *B* cations once again filling the octahedral sites. This results in a structure composed of infinite chains of face sharing $[BO_6]$ octahedra extending along the *c* axis separated by chains of *A* cations. The general 2H-hexagonal perovskite related oxides deviate from the standard 2H-perovskite in that the AB packing is now composed of a tripled $[AO_3]$ layer, $[A_3O_9]$, and a modified $[A_3O_9]$ layer, $[A_3A'O_6]$. This stacking leads to chains of alternating face sharing $[BO_6]$ octahedra and $[A'O_6]$ trigonal prisms extending down the *c* axis separated by chains of *A* cations. The general formula is given by $A_{3n+3m}A'_nB_{3m+n}O_{9m+6n}$ where *n* is the number of $[A_3A'O_6]$ layers and *m* is the number of $[A_3O_9]$ layers. $(La_{2.47}Na_{0.53})NaRhO_6$, $(Pr_{2.45}Na_{0.55})NaRhO_6$, $(Nd_{2.45}Na_{0.55})NaRhO_6$, $(La_2Na)NaPtO_6$ and $(Nd_2Na)NaPtO_6$ have structures that consist solely of AB stacked $[A_3A'O_6]$ layers and, within these layers, the Na^+ cation occupies all of the *A'* site and partially substitutes for the rare earth cations on the *A* site. Thus sodium is also present in the chains of cations that separate the face-sharing octahedra/trigonal prism chains.

Two different flux preparation methods were used in the growth of the $(A_{3-x}Na_x)NaBO_6$ (A = La, Pr, Nd; B = Rh, Pt) crystals. The first involved the growth of single crystals from a "wet" hydroxide flux resulting in $La_{2.47}Na_{1.53}RhO_6$, $La_2Na_2PtO_6$ and $Nd_2Na_2PtO_6$. The second method, using a Na_2CO_3 flux, produced $Pr_{2.45}Na_{1.55}RhO_6$ and $Nd_{2.45}Na_{1.55}RhO_6$ crystals as well as poorer quality $(La_{3-x}Na_x)NaRhO_6$ crystals. In both cases, the RE_2O_3 was initially heated to 1000 ºC for 15 h to ensure dryness. Pr_2O_3 was obtained from Pr_6O_{11} by heating it in a tube furnace under flowing $H_2(5\%)/N_2(95\%)$ at 1000 ºC for 15 h, cooling it, grinding it up, then heating it again at 1000 ºC for another 15 h under flowing $H_2(5\%)/N_2(95\%)$. The RE_2O_3 (RE = La, Pr, Nd) was stored in a vacuum desiccator when not in use. Rhodium metal was used to grow $Pr_{2.45}Na_{1.55}RhO_6$ and $Nd_{2.45}Na_{1.55}RhO_6$ while Rh_2O_3 (prepared by heating powdered Rh metal at 1000 ºC for 24 h in air) was used for $La_{2.47}Na_{1.53}RhO_6$.

$(A_{3-x}Na_x)NaBO_6$ (A = La, Pr, Nd; B = Rh, Pt) were all found to crystallize in the trigonal space group $R\ \bar{3}c$ with the K_4CdCl_6 structure. Based on the concept of charge neutrality the overall contribution of the cation charges in $(A_{3-x}Na_x)NaBO_6$ (A = La, Pr, Nd; B = Rh, Pt) must sum to +12 to offset the six O^{2-} anions. In the case of the Pt containing analogues and assuming Na has a +1 charge and the rare earth has +3 charge this results in Pt^{4+} cations. Assuming standard charges of the rare earth and the sodium cations and given the constraints used in the single crystal refinement process, the Rh containing crystals contain a charge discrepancy suggesting the presence of a small amount of Rh^{4+} amongst the predominantly Rh^{3+} cations with overall Rh charges of +3.06, +3.10 and +3.10 for the La, Pr and Nd analogues, respectively. Alternately, the refined site occupancies on the A site may be slightly off accounting for the observed discrepancy. It is worth noting that it is only on account of the mixing of the +3 rare earth cations and the Na^+ cations on the A site that the rare earth cations are able to occupy the site.

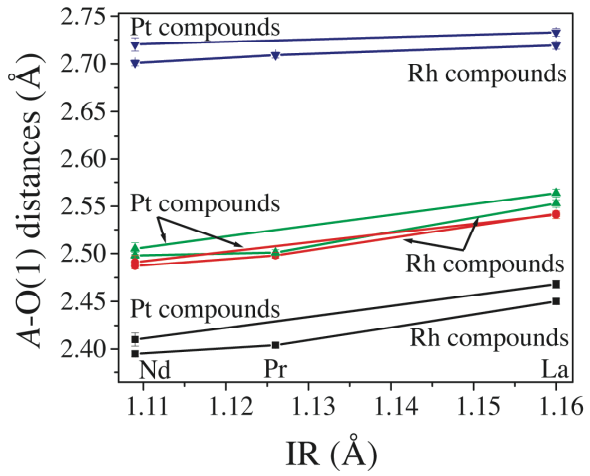

Figure 8. *A-O(1) bond distances for $(A_{3-x}Na_x)NaBO_6$ (A = La, Pr, Nd; B = Rh, Pt).*

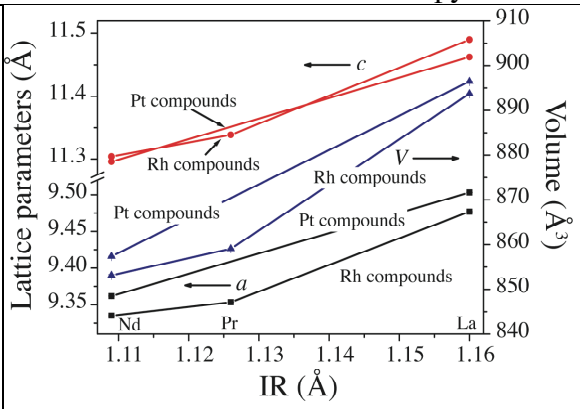

Figure 9. *Lattice parameters and volume of $(A_{3-x}Na_x)NaBO_6$ (A = La, Pr, Nd; B = Rh, Pt) as a function of rare earth cation size.*

The similarity in size between the Na^+ (ionic radius 1.02 Å) and La^{3+} (1.03 Å), Pr^{3+} (0.99 Å), and Nd^{3+} (0.98 Å) cations helps facilitate the mixing. Given that the only other cations found to substitute onto the A site are Ca^{2+} (ionic radius 1.00 Å), Sr^{2+} (1.18 Å) and Ba^{2+} (1.35 Å) this suggests not only a charge constraint but also a size limit on what cations are suitable.

Exploration of other divalent cations such as Pb^{2+} (ionic radius 1.19 Å), Ag^{2+} (0.94 Å) and mixed mono/trivalent combinations of approximately the same size may lead to new compounds. In Figures 8 and 9, the trends in bond lengths and lattice parameters are shown.

Crystal Growth and Single Crystal Structures of *RE*RhO_3 (*RE* = La, Pr, Nd, Sm, Eu, Tb)

Single crystals of $LaRhO_3$, $PrRhO_3$, $NdRhO_3$, $SmRhO_3$, $EuRhO_3$ and $TbRhO_3$ were grown for the first time using a K_2CO_3 flux. All the compounds were found to crystallize in the orthorhombic space group *Pbnm* (No. 62) and adopt the $GdFeO_3$ distorted perovskite structure type. Transition towards a pseudo cubic cell is noted as the rare earth cation size increases. To grow the crystals, the reactants were placed in an alumina crucible and covered with anhydrous K_2CO_3, acting here, as a flux. The crucible was covered with an alumina lid and heated in a tube furnace from room temperature to 1050 ºC at a rate of 600 ºC/h, held at 1050 ºC for 24 h, then cooled to 800 ºC at a rate of 15 ºC/h, held at 800 ºC for 1 h, then step cooled to room temperature by removing power to the furnace elements.

While reactions were performed with all the lanthanides (except Pm) only La, Pr, Nd, Sm, Eu and Tb produced crystals of a quality suitable for structural analysis by single crystal X-ray diffraction. Figure 10 shows a scanning electron micrograph of a $LaRhO_3$ single crystal (approx. 33 µm across) with truncated octahedral geometry, i.e., six four sided faces and eight six sided faces, consistent with the orthorhombic space group *Pbnm*. The majority of unsuccessful reactions resulted in large, flaky, black hexagonal crystals (up to 10 mm across and typically less than 0.5 mm thick) with an approximate ratio of elements 1K: 2Rh: 6O (obtained from EDS measurements) that were not suitable for single crystal measurements.

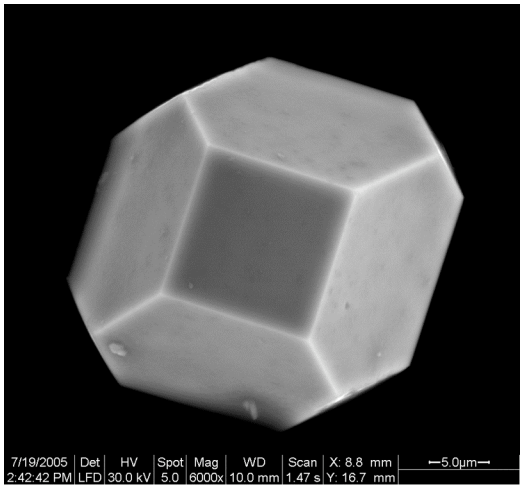

Figure 10. *Scanning electron micrograph of a $LaRhO_3$ single crystal (truncated octahedron $4^6 6^8$, Pbnm).*

The structure is shown in Figure 11 and a comparison is made to the undistorted cubic perovskite structure.

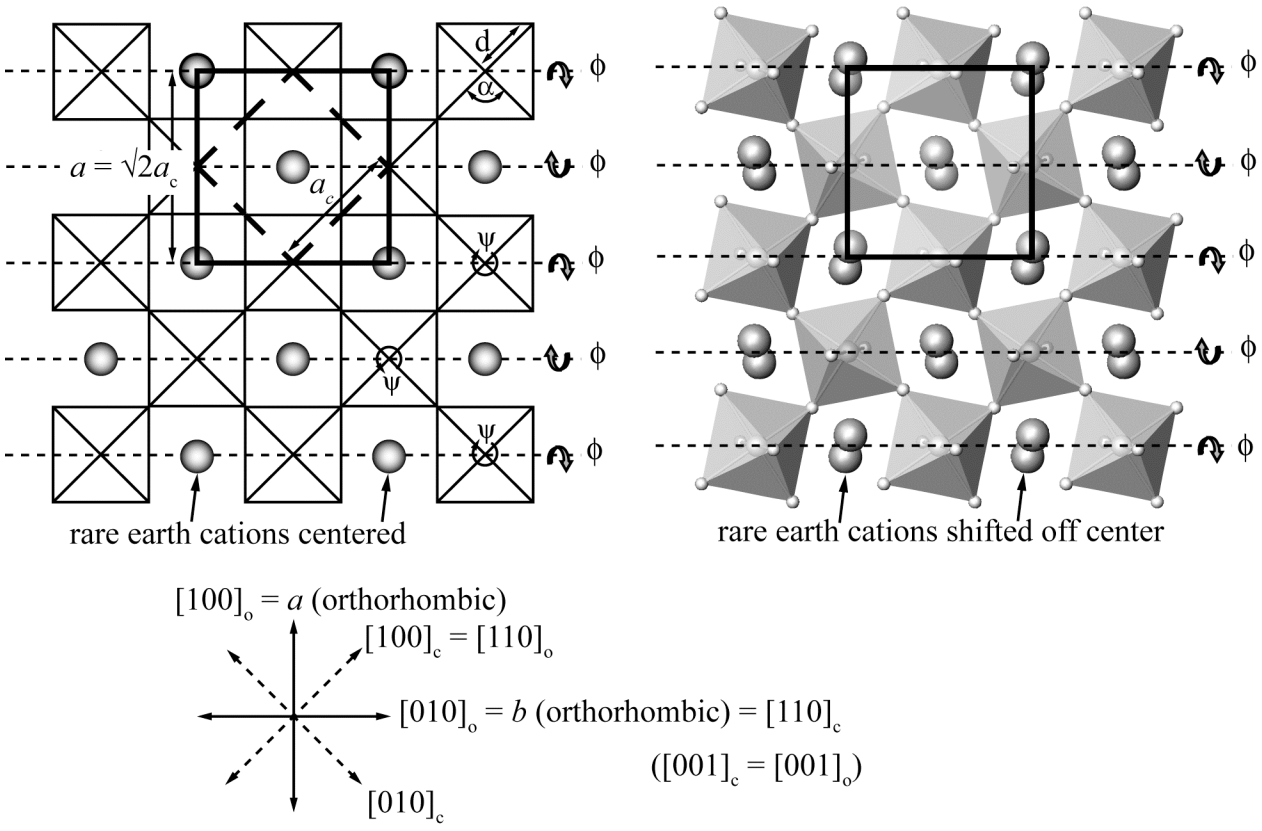

Figure 11. *Comparison of the unit cell of the cubic aristotype (bold, dashed) and the undistorted orthorhombic perovskite hettotype (bold, solid). In the ideal perovskite* $a = \sqrt{2}a_c$. *Distortion of the perovskite structure from Pm* $\bar{3}$ *m to Pbnm results in a new unit cell* $a \approx \sqrt{2}a_c < b \approx \sqrt{2}a_c$ *and* $c = 2a_c$ *due to octahedral tilting about the* $[010]_o$ *and* $[001]_o$ *axes (*ϕ *and* ψ*, respectively) and distortion of the regular octahedra so that the octahedral metal-oxygen bond lengths (d) vary and the oxygen-metal-oxygen bond angles (*α*) in the equatorial plane diverge from 90°. The rare earth cation is displaced away from the center of the cubo-octahedral cavity formed by the corner linked octahedra (12-fold oxygen coordination) resulting in an 8-fold coordination environment. The distorted perovskite structure (Pbnm) is shown on the right. Note the rotation in the opposite direction of corner linked octahedra.*

Structural Studies of Sr_2GaSbO_6, Sr_2NiMoO_6, and Sr_2FeNbO_6 Using Pressure and Temperature

We completed our work on Sr_2GaSbO_6, Sr_2NiMoO_6, and Sr_2FeNbO_6 using pressure and temperature. A phase transition, where the unit cell changes symmetry from tetragonal to cubic, is observed for each compound at elevated temperatures. The phase transition changes the structure from one exhibiting an octahedral tilting distortion at ambient temperature to one that is untilted above the transition temperature. At elevated pressures the $c/\sqrt{a}$ lattice parameter ratio increases, indicating that the magnitude of the octahedral tilting distortion is increasing as a function of pressure. In the pressure range studied, up to ~6 GPa, no phase transitions were observed.

Polycrystalline Sr_2NiMoO_6 and Sr_2FeNbO_6 were prepared by conventional solid state techniques, whereas Sr_2GaSbO_6 was prepared in a $SrCl_2$ flux with 2:1 flux to sample ratio. The samples were annealed with intermediate grinding and heating cycles until no more changes were evident in the diffraction peaks. Phase purity was established by powder X-ray diffraction using a Rigaku D/Max 2100 diffractometer. Approximately 2% of a secondary $SrMoO_4$ phase was observed in the synthesis of Sr_2NiMoO_6. *In situ* high temperature X-ray powder diffraction measurements with Cu K_α radiation were performed using a Rigaku D/MAX 2100 diffractometer with a Rigaku high-temperature attachment. The polycrystalline samples were mounted in a steel sample holder and the measurements were performed under flowing nitrogen. Diffraction data were collected from 15-110° 2θ in 0.04° steps at each temperature interval. A sample was allowed to equilibrate at each temperature for 30 minutes before data collection commenced. Diffraction data analysis was performed using the FullProf software program. A Thompson-Cox-Hastings pseudo-Voigt function was used to model the peak shapes in the angular range 15-110° 2θ. The standard uncertainties are those reported by the software and may underestimate the uncertainty.

In situ high pressure synchrotron X-ray powder diffraction experiments were performed using a diamond anvil cell (DAC) at the X7A beam-line at the National Synchrotron Light Source (NSLS) at Brookhaven National Laboratory (BNL). The primary white beam from the bending magnet was monochromated using a channel-cut Ge (111) monochromator after a set of slits defining the beam size compatible with the size of the sample chamber inside the DAC. A gas-proportional position-sensitive detector (PSD) was stepped in 0.25° intervals over the angular range of 5–35° in 2θ with counting times of 50–100 s per step. The wavelength of the incident beam, PSD zero channel and PSD degrees/channel were determined from a CeO_2 standard (SRM 674). Polycrystalline samples were loaded into the DAC at ambient pressure and room temperature along with a few small ruby chips. A methanol-ethanol-water mixture with component ratio of 16:3:1 was used as the hydrostatic pressure-transmitting medium. The DAC is based on a modified Merrill-Bassett design and employs two diamonds with 0.5 mm diameter culets on tungsten-carbide supports. The X-rays are admitted by a 0.5 mm diameter circular aperture, and the exit beam leaves via a 0.5×3.0 mm rectangular tapered slit, oriented perpendicular to the horizontal plane of the diffractometer. The sample chamber is outfitted by a ≈60-80 μm diameter hole made using a spark-erosion method in the center of a 250 μm thick stainless-steel gasket, pre-indented to 100 μm thickness before erosion. The DAC was placed on the second axis of the diffractometer, and the sample position was adjusted using a pre-centered microscope. The pressure at the sample was measured by detecting the shift in the R1 emission line of the included ruby chips. No evidence of nonhydrostatic conditions or pressure anisotropy were detected during our experiments, and the R1 peaks from three included ruby chips remained strong and sharp with deviations in the measured pressure of less than 0.2 GPa. Room temperature diffraction patterns were collected using a wavelength of 0.62245 Å. Diffraction data analysis was performed using the EXPGUI interface of GSAS. A pseudo-Voigt function was used to model the peaks in the range employed in the refinements from 6° to 35° 2θ, excluding the regions which contained strong Bragg peaks from the pressure cell gasket.

Analysis of laboratory X-ray diffraction data show that Sr_2GaSbO_6, Sr_2NiMoO_6, and Sr_2FeNbO_6 crystallize in a tetragonal unit cell with $a \approx b \approx 5.6$ Å and $c \approx 7.9$ Å. Structure refinements were performed at ambient temperature and pressure with space group $I4/m$ for Sr_2GaSbO_6 and Sr_2NiMoO_6, which is in agreement with previous structural studies. We found

that space group *I4/mcm* best described the symmetry of Sr_2FeNbO_6. The ordered double perovskites with space group *I4/m* belong to a subgroup of the aristotype perovskite space group $Pm\bar{3}m$, and may be obtained via the combination of the irreducible representations R_1^+ and R_4^+ for cation ordering and out of phase octahedral tilting, respectively. The disordered perovskite with space group *I4/mcm* belongs to a subgroup that may be obtained via the irreducible representation R_4^+ of the aristotype perovskite space group $Pm\bar{3}m$.

Sr_2GaSbO_6

Inspection of the X-ray diffraction data collected above ambient temperature revealed changes in the patterns that are noticeable in the high 2θ range. At higher temperature, these peaks begun to coalesce, and at 723 K each becomes a single peak near 94° and 103°. The systematic absences of the X-ray diffraction pattern at 723 K up to 873 K are indicative of a cubic space group with $a \approx 7.87$ Å. An ordered double perovskite with space group $Fm\bar{3}m$ was used in the Rietveld refinement of the data collected between 723-873 K.

Sr_2NiMoO_6

Inspection of the X-ray diffraction data of Sr_2NiMoO_6 collected above ambient temperature showed changes in the patterns that were visible in the high 2θ range that were similar to those found for Sr_2GaSbO_6. The phase transition occurs above 523 K, which is in agreement with the temperature of 503 K that was suggested previously; the small difference between the transition temperatures may be related to different synthetic conditions or degree of cation ordering. The high temperature structure of Sr_2GaSbO_6 was refined in space group $Fm\bar{3}m$.

Sr_2FeNbO_6

The ambient temperature X-ray diffraction pattern of Sr_2FeNbO_6 was examined and could be indexed as tetragonal with $a \approx 5.60$ Å and $c \approx 7.96$ Å. Inspection of the X-ray diffraction data of Sr_2FeNbO_6 collected above ambient temperature showed changes in the patterns that were visible in the high 2θ range and that were similar to those found for Sr_2NiMoO_6 and Sr_2GaSbO_6. The high temperature structure was refined in space group $Pm\bar{3}m$. Unlike both Sr_2NiMoO_6 and Sr_2GaSbO_6, where a contraction of the *c* lattice parameter is evident with an increase in temperature, the *c*-axis in Sr_2FeNbO_6 increases with temperature. The *a* lattice parameter also smoothly increases with temperature.

High Pressure

The high-pressure structural behavior of simple perovskites (ABO_3) has been examined in terms of the relative compressibility of the AO_{12} and BO_6 polyhedra. If the AO_{12} is more compressible than the BO_6 polyhedra, the structure may become more distorted with pressure, which has been observed in $CaSnO_3$. If the AO_{12} is less compressible than the BO_6 polyhedra, the structure may become less distorted with pressure, which has been observed in $GdAlO_3$ and $GdFeO_3$. Furthermore, pressure may induce a phase transition to a higher symmetry space group as was observed, for example, in $LaAlO_3$, or it may induce a phase transition to a lower

symmetry space group as was observed, for example, in Ba_2YTaO_6. If there is a phase transition present in the compounds of this study, then two possible pressure-induced phase transitions are from *I*4/*m* to $P2_1/n$ or from *I*4/*m* to $Fm\bar{3}m$, corresponding to the case where the structure becomes more distorted with pressure, and the case where it becomes less distorted with pressure, respectively.

The diffraction patterns of Sr_2NiMoO_6, Sr_2GaSbO_6, and Sr_2FeNbO_6 exhibited substantial peak broadening with increasing pressure. Rietveld refinements of the structures were attempted, but resulted in large uncertainties in the atomic positions and unphysical changes in bond distances with changes in pressure. The small X-ray scattering cross section of oxygen compared to the heavy cations, the peak broadening that occurs as the pressure is increased, and the reduced number of reflections in the limited angular range, all prevent a full structure refinement. A LeBail method analysis was used to obtain the lattice parameters in the ordered double perovskite structure, where the space group *I*4/*m* was used for Sr_2NiMoO_6 and Sr_2GaSbO_6, while the space group *I*4/*mcm* with a disordered cation arrangement was used for Sr_2FeNbO_6. A least squares fit was used to determine the linear pressure dependence of the lattice parameters. The $c/\sqrt{a}$ ratio increases with an increase in pressure, which has been shown to correlate with an increase in the magnitude of the octahedral tilting distortion. This implies that the structure becomes more distorted with pressure and that, therefore, the *I*4/*m*-$Fm\bar{3}m$ phase transition may be ruled out.

In a phase transition that also changes the octahedral tilting type, the resulting changes in the diffraction pattern may be weak and subtle and, therefore, difficult to separate from the background noise; the situation is further complicated by the peak broadening at higher pressures. A hypothetical crystal structure of a perovskite crystallizing with space group $P2_1/n$ was generated using SPuDS. The fractional coordinates were retained and the lattice parameters were refined. This approach has the advantage that it is a rapid method to generate the approximate peak intensities which result from the in-phase tilting and A-site displacements. The calculated peak intensities of the reflections allowed in $P2_1/n$ using this method are of a similar magnitude as the noise of the background. Although no obvious additional reflections were observed that could be associated with in-phase tilting or A-site cation displacements, these weak reflections could have been missed and, therefore, an analysis of the peak splitting for Sr_2NiMoO_6 was also undertaken. The peak near 22.5° 2θ was examined in detail, since it would be expected to split from a doublet of 024 and 132 in space group *I*4/*m*, to a quartet 204, 20-4, 132, 13-2 in space group $P2_1/n$. Although there are clearly two peaks at low pressures, the pressure-induced peak broadening obscures simple analysis of the peak splitting. Similar results were also found for both Sr_2GaSbO_6 and Sr_2FeNbO_6; therefore these compounds all appear to retain tetragonal symmetry in the pressure range examined. It is possible that higher pressures may induce a phase transition and that the technique described above may be used to investigate phase transitions in perovskites.

In this study we were able to shown that the application of pressure induces a more rapid change in the *a*-lattice parameter than in the *c*-lattice parameter, which is indicative of an increase in the magnitude of the octahedral tilting distortion. There was no indication for a pressure induced phase transition up to 5.7 GPa in Sr_2NiMoO_6, Sr_2GaSbO_6, and to 2.7 GPA Sr_2FeNbO_6. Their bulk moduli are similar to those of other Sr-containing ordered double perovskites. We have structurally characterized the temperature induced phase transition that Sr_2NiMoO_6, Sr_2GaSbO_6, and Sr_2FeNbO_6 exhibit near 523 K, 673 K, and 573 K, respectively.

Upon heating, Sr_2NiMoO_6 and Sr_2GaSbO_6 undergo a phase transition from *I*4/*m* to *Fm*-3*m* and Sr_2FeNbO_6 undergoes a phase transition from *I*4/*m* to *Pm*-3*m*; concomitantly, the octahedral tilting distortion changes from an antiphase tilting ($a^0a^0c^-$) to an untilted form ($a^0a^0a^0$) in each case. The changes in cell parameters and unit cell volumes are indicative of a continuous phase transition.

Several new palladates, *Ln*$KPdO_3$ (*Ln* = La, Pr, Nd, Sm – Gd), were grown as single crystals and structurally characterized.

The ability to substitute elements for one another in oxides is known for virtually every structure type where, in general, the two most important factors for a given chemical substitution are the size and charge of the constituent cations. In this regard, platinum group metals make excellent substitutes for each other in many structure types because they are very similar in size for a given oxidation state and, furthermore, are able to assume a wide range of oxidation states. An excellent example demonstrating this interchangeability of platinum group metals can be found in the lanthanide containing double perovskite osmates, ruthenates and iridates with the general formula, $Ln_2MM'O_6$ (*Ln* = La, Pr, Nd, Sm, Eu; *M* = Li, Na; *M′* = Ru, Os, Ir). Similarly, in the 2H-perovskite related oxides described by the general formula $A_{3n+3m}A'_nB_{3m+n}O_{9m+6n}$, a wide variety of platinum group metals, including platinum, rhodium, iridium and palladium, can substitute on the *B*-site and result in compositions such as Sr_4PtO_6, Sr_4PdO_6, Ca_4PdO_6, and Ca_3MgIrO_6, to name a few.

Other substitutions are more complex and involve the exchange of two divalent cations by one monovalent and one trivalent cation. For example, $(NaLa_2)NaPtO_6$ was the first example of a 2H-perovskite related oxide in which the *A*-site substitution of an alkaline earth metal cation by a lanthanide and an alkali metal cation was accomplished. Since then, several other *A*-site substituted 2H-perovskite related oxides with the general formula $(A_{3-x}Na_x)NaBO_6$ (*A* = La, Pr, Nd; *B* = Rh, Pt) have been reported by us. Similarly, the oxide $Gd_{0.96}Na_{1.04}IrO_4$ is related to Ca_2IrO_4, via the substitution of two calcium cations for one gadolinium and one sodium cation. In that series, $Ln_{1-x}Na_{1+x}IrO_4$ (*Ln* = Gd – Er, Y; *x* = 0.04 - 0.25), it is interesting to note that the composition adjusts itself in an attempt to maintain a constant unit cell volume (Ln^{3+} (1.00 – 0.945 Å) and Na^+ (1.12 Å)). There are, thus, several complex substitutions that can be achieved, including ($2Ca^{2+} = Ln^{3+} + Na^+$), ($2Sr^{2+} = Ln^{3+} + K^+$) and ($2Ba^{2+} = Ln^{3+} + K^+$) for differently sized lanthanides. Traditionally, to achieve such compositional changes one has relied on solid state powder synthesis to prepare materials with new compositions, where one or more of the constituent elements from a previously prepared and structurally characterized phase have been substituted.

We have been interested in the discovery of new materials through crystal growth, where we have focused our efforts on studying the reactivity of lanthanide and platinum group metals in alkali metal hydroxides as a means of growing high quality single crystals of new oxide materials. Within this group of platinum group metal oxides, the chemistry of new palladates grown from alkali metal hydroxides remains relatively unexplored. Several years ago, we reported the hydroxide flux synthesis of $CaPd_3O_4$ and $SrPd_3O_4$ and more recently, we succeeded in synthesizing $LuNaPd_6O_8$, a new material structurally related to the APd_3O_4 (*A* = Ca, Sr)

phases, from a sodium hydroxide flux. Interestingly, $LuNaPd_6O_8$ represents the first example of an ordered substitution of a lanthanide metal and an alkali metal for an alkaline earth metal on the *A*-site of a platinum group metal oxide and also the first palladate to contain both a lanthanide and an alkali metal. In an effort to further explore the chemistry of palladium in hydroxide fluxes, we have prepared a new series of ordered, lanthanide and alkali metal containing palladates, $LnKPdO_3$ (*Ln* = La, Pr, Nd, Sm – Gd) and a partially copper substituted analog, $PrK(Cu_{0.14}Pd_{0.86})O_3$ from potassium hydroxide fluxes. For this structural series we essentially modified the A_2MO_3 (*A* = Ca, Sr, Ba; *M* = Cu, Pd) alkaline earth metal palladates and cuprates where we took advantage of the ($2Ba^{2+} = Ln^{3+} + K^+$) type substitution.

Golden brown, needle-shaped single crystals of $LnKPdO_3$ (*Ln* = La, Pr, Nd, Sm – Gd) and $PrK(Cu_{0.14}Pd_{0.86})O_3$ were grown from molten potassium hydroxide fluxes. La_2O_3, Pr_2O_3, Nd_2O_3, Sm_2O_3, Eu_2O_3, or Gd_2O_3, Pd metal, and KOH were loaded into alumina or silver crucibles and covered. In the case of $PrK(Cu_{0.14}Pd_{0.86})O_3$, CuO was utilized as the source of copper. The crucibles were placed into a programmable box furnace and heated to 750 °C in 2 hours, held at that temperature for 5 h and then cooled to 600 °C in 36 h. The reaction was allowed to cool to room temperature by shutting off the furnace. The crystals were removed from the flux matrix by dissolving the flux in water and isolating the crystals by vacuum filtration.

The new palladates are structurally related to the A_2MO_3 (*A* = Ca, Sr, Ba; *M* = Cu, Pd) alkaline earth metal palladates and cuprates and the crystal structure of $LnKPdO_3$ is shown in Figures 12-13.

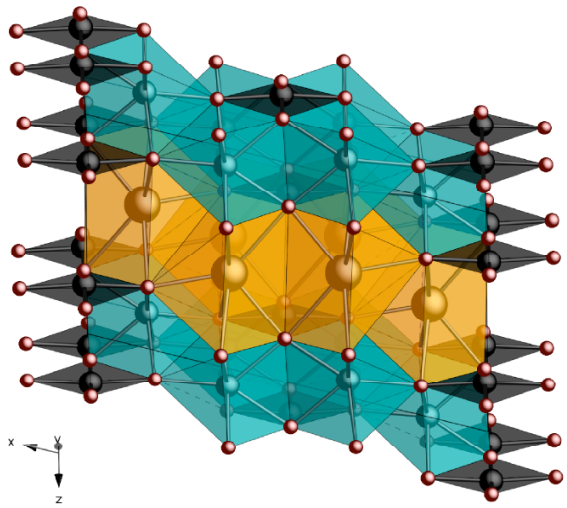

Figure 12: *Structural representation of $LnKPdO_3$ with LnO_7 capped trigonal prisms shown in teal, KO_7 capped trigonal prisms in orange, and PdO_4 square planes shown in black. Oxygen atoms are represented as red spheres.*

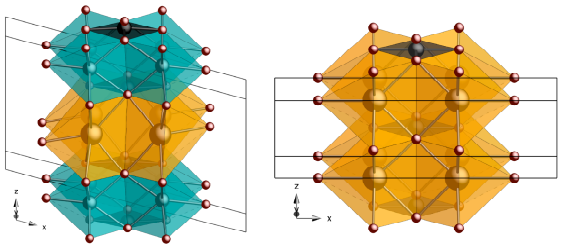

Figure 13: *The face-shared chains along the z-direction of LnO_7-KO_7-LnO_7 capped trigonal prisms are shown in (a) and for comparison the BaO_7-BaO_7 face-shared capped trigonal prisms of the structurally related phase, Ba_2PdO_3 are shown in (b).*

The structure contains ordered slabs of Ln^{3+} and K^+ in a seven coordinate environment and Pd^{2+} atoms in a square planar coordination environment. In each slab, there are six LnO_7 or KO_7

capped trigonal prisms; four centrally located and one located at each edge of the unit cell along the *x*-direction of the slab. The four centrally located LnO_7 or KO_7 capped trigonal prisms edge-share with each other and corner-share with the apical oxygen of the cap of the additional LnO_7 or KO_7 capped trigonal prisms near the edge of the cell along the *x*-direction. The LnO_7 and KO_7 capped trigonal prisms further connect via the sharing of one triangular face along the *z*-direction to form infinite chains of LnO_7-KO_7-LnO_7 polyhedra. Fig. 13 shows a comparison of the chains running along the *z*-direction for both the (a) $LnKPdO_3$ structure and the (b) Ba_2PdO_3 structure. The square planar coordination environment of the palladium atoms is slightly distorted from ideal in that, the square planes are made up of two equivalent and two nonequivalent Pd-O bond lengths. The PdO_4 square planes are situated perpendicular to the *z*-direction and occupy the space created in the middle of four of the LnO_7 and KO_7 capped trigonal prisms. The complex connectivity of the capped trigonal prisms leads to an evenly spaced distribution of PdO_4 square planes along the *x*- and *y*-directions with the distance between palladium atoms equal to the *a* and *b* lattice parameters, respectively. However, because the Ln^{3+} cation and the K^+ cation are of unequal size, the palladium atoms along the *z*-direction are unevenly spaced. The Pd – Pd distances vary as a function of the size of the lanthanide and, as the size of the lanthanide decreases, the distance between the palladium atoms decreases as well.

$LnKPdO_3$ (*Ln* = La, Pr, Nd, Sm – Gd) and $PrK(Cu_{0.14}Pd_{0.86})O_3$ differ from the A_2MO_3 (*A* = Sr, Ba) phases, in that in place of two Sr^{2+} or Ba^{2+} cations, an ordered, 1:1 arrangement of Ln^{3+} and K^+ cations is observed. The overall charge on the *A*-site remains +4, but is maintained by one Ln^{3+} and one K^+ atom. The general formula $AA'MO_3$, where *A* and *A′* are two divalent cations or the combination of one trivalent and one monovalent cation can be utilized to describe the stoichiometry. As a result of this ordered cation substitution, the *c*-parameter effectively doubles, a reduction in symmetry is observed, and the space group changes from orthorhombic (*Immm*) to monoclinic (*C*2/*m*). The reduction in symmetry and ordering can be attributed to the significant size and charge difference of the Ln^{3+} and K^+ cations, where the Ln^{3+} cation (1.06 – 1.00 Å) is much smaller than K^+ (1.46 Å) [32] and most likely the dominant force of cation ordering.

When analyzing the structural relationship between the A_2PdO_3 (*A* = Sr, Ba) and the $LnKPdO_3$ (*Ln* = La, Pr, Nd, Sm – Gd) compositions, we can consider the existence of a structure stability limit based on the size of the *A*-cations. The Ba_2PdO_3 phase roughly represents the upper limit of stability, since barium is the largest alkaline earth metal and Sr_2PdO_3 roughly represents the lower limit, since the A_2PdO_3-type structure does not form for Ca^{2+}, for which the cubic $CaPd_3O_4$ phase is observed. The ionic radii of Ba^{2+} and Sr^{2+} cations in a seven coordinate environment are 1.38 Å and 1.21 Å, respectively; therefore, the range of the average ionic radii on the *A*-site of the $LnKPdO_3$ (1.26 Å – 1.23 Å) phases ideally falls between 1.38 Å and 1.21 Å.[32] In the $LnKPdO_3$ phases, the two divalent *A*-cations have been replaced by one trivalent *A*- and one monovalent *A′*-cation giving the general formula $AA'PdO_3$. The primary structural difference between A_2PdO_3 and the $AA'PdO_3$ structures is the effective doubling of the *c*-parameter, thus we can roughly estimate the cell volume of A_2PdO_3 (*A* = Sr, Ba) in the monoclinic $AA'PdO_3$ structure from the lattice parameters if we double the *c*-parameter in the orthorhombic cell. Unlike the $Ln_{1-x}Na_{1+x}IrO_4$ (*Ln* = Gd – Er, Y) structure, where a relatively constant cell volume is maintained by adjusting the sodium content to counter the effect the size of the smaller lanthanide cations has on the structure, the $LnKPdO_3$ structure appears to accommodate a range of cell volumes while maintaining a 1:1 order of the Ln^{3+} and K^+ cations.

The partial substitution of copper in place of palladium in the $PrK(Cu_{0.14}Pd_{0.86})O_3$ phase is interesting, in that, only a small percentage of copper ended up in the structure. We postulated that because of the existence of isostructural A_2CuO_3 (A = Ca, Sr, Ba) phases and the copper-palladates, $Sr_2(Pd_{1-x}Cu_x)O_3$ ($0 \leq x \leq 1$), that perhaps, an ordered $LnKCu_{0.5}Pd_{0.5}O_3$ structure would result. However, because copper is readily dissolved in hydroxide fluxes and forms very stable phases in the presence of lanthanides, it appears that there may be a kinetic competition for the copper and thus only a small percentage of copper was substituted into the $PrK(Cu_{0.14}Pd_{0.86})O_3$ structure.

We have investigated the low temperature structural phase transition of $Ba_3NaIr_2O_9$ in more detail. Single crystal X-ray and synchrotron X-ray powder diffraction have been used to probe the structure of $Ba_3NaIr_2O_9$ from 300 K down to 20 K. $Ba_3NaIr_2O_9$ is found to undergo a continuous phase transition from the hexagonal space group $P6_3/mmc$ to the monoclinic space group $C2/c$ at ~ 190 K.

Numerous researchers have investigated iridium double and triple perovskites where the iridium is known to take on oxidation states of +4, +5 and +6. We have recently published the structures and magnetic properties of the iridium triple perovskite, $Ba_3NaIr_2O_9$. To investigate the low temperature structure, we carried out low temperature X-ray diffraction experiments at the National Synchrotron Light Source (NSLS) at Brookhaven National Laboratory (BNL). We observed that $Ba_3NaIr_2O_9$ underwent a structure transition and proceeded to determine its structure. Triple perovskites are know to undergo low temperature structure transitions from the room temperature $P6_3/mmc$ structure to an orthorhombic structure in the space group $Cmcm$, for example in $Ba_3CoRu_2O_9$ and $Ba_3NaRu_2O_9$, or to a monoclinic structure in space group $C2/c$, as in $Ba_3NdRu_2O_9$. Based on our data we conclude the existence of a $P6_3/mmc$ to $C2/c$ structure transition in $Ba_3NaIr_2O_9$.

$Ba_3NaIr_2O_9$ was synthesized by flux growth: Ir powder, $Ba(OH)_2 \bullet 8H_2O$, and NaOH were placed in a 12.5 mm diameter silver tube that had been sealed at one end and which was crimped at the other end. The silver tube was placed into a box furnace and heated to the reaction temperature of 650 °C at 50 °C/h, held there for 12 hours, and then cooled to room temperature by turning off the furnace. The crystals were extracted from the flux matrix by sonication in methanol.

Single crystal X-ray diffraction measurements were collected using a Bruker SMART APEX CCD-based diffractometer (Mo K_α radiation, λ = 0.71073 Å) with a cryo attachment allowing measurements down to 100 K. A black crystal was epoxied onto a thin glass fiber and an initial measurement was collected at 300 K with sufficient time for full crystal structure determination. Following this, shorter collection time measurements were performed in 10 K steps from 300 K down to 140 K then at 120 and 100 K. These were done in order to observe any changes in lattice dimensions as a function of temperature. A second full crystal structure determination at 230 K was also performed. All single crystal structure determinations were preformed using the Bruker suite of software.

High resolution X-ray powder diffraction measurements were performed on beamline X7A at the NSLS (National Synchrotron Light Source) at Brookhaven National Laboratories using a sample of finely ground single crystals. Variable temperature measurements (at 300, 200, 100, 20 K) were collected using a closed cycle cryofurnace with monochromatic radiation of wavelength λ = 0.71016 Å and a step size of 0.01° (2θ angle). Samples were housed in a glass capillary of radius 0.3 mm. The capillary was rotated continuously in the cryostat to minimize preferred orientation. Structural models were refined by the Rietveld method as implemented in the program Rietica.

Structure measurements of the single crystal X-ray diffraction pattern of $Ba_3NaIr_2O_9$ showed that at 300 K it adopts a hexagonal symmetry in space group $P6_3/mmc$. Atomic coordinates and lattice parameters derived from the single crystal measurements. Reports of a low temperature phase in the analogous $Ba_3NaRu_2O_9$ prompted a study of the structure using variable temperature powder synchrotron diffraction techniques. The X-ray powder diffraction pattern of $Ba_3NaIr_2O_9$ collected at 300 K refines well in space group $P6_3/mmc$. As the temperature is decreased the hexagonal symmetry is lost and below 200 K the structure adopts a monoclinic symmetry in space group $C2/c$. A similar result was reported for $Ba_3NdRu_2O_9$.

At 300 K the hexagonal model, space group $P6_3/mmc$, provides a good fit for the data but at 200 K the monoclinic model, space group $C2/c$, yields better refinement statistics. However, close inspection of the peak splitting, Figures 14 and 15, show that monoclinic reflections do not occur at 200 K suggesting that the improved fit of the monoclinic model over the hexagonal model at 200 K is due to the increased number of refinable parameters in the lower symmetry space group.

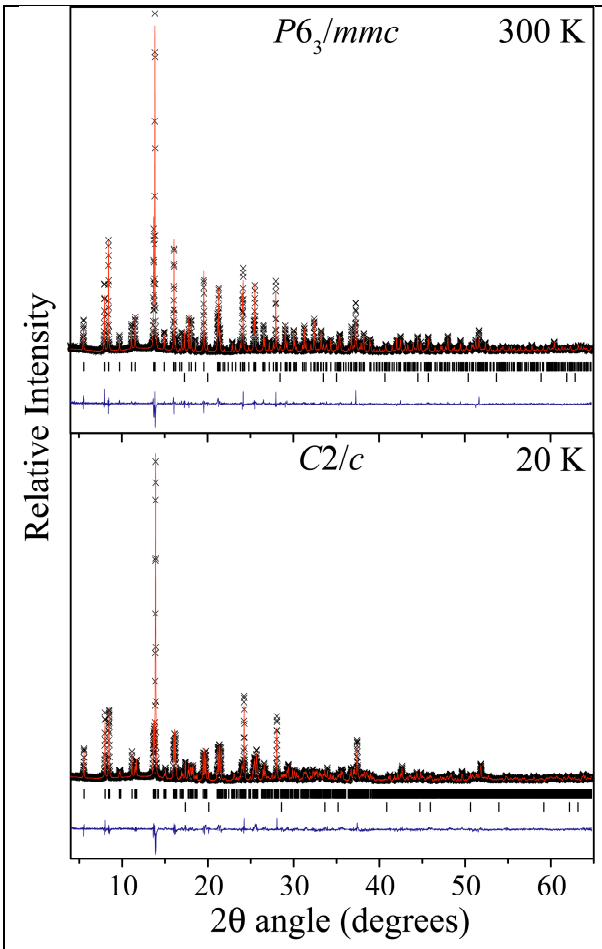

Figure 14: *Sample synchrotron powder diffraction patterns of $Ba_3NaIr_2O_9$ at 300 and 20 K. The crosses show the observed data, the red line the calculated pattern and the blue line at the bottom the difference between the observed and the calculated patterns. The first set of vertical reflection markers corresponds to the primary phase ($P6_3/mmc$ at 300 K and C2/c at 20 K) and the second set to a silver impurity phase.*

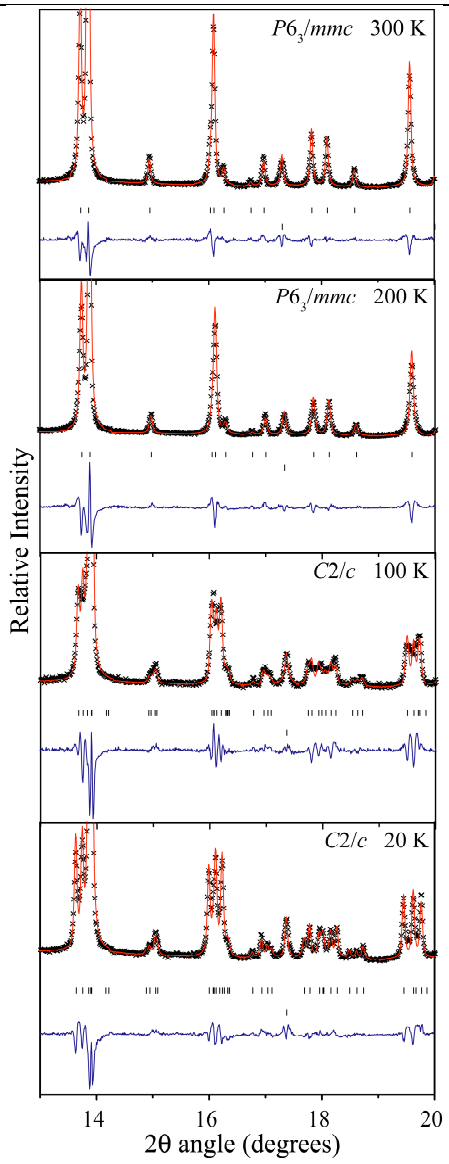

Figure 15: *Enlarged portions of the synchrotron X-ray diffraction patterns of $Ba_3NaIr_2O_9$ at various temperatures. The crosses indicate the data points and the top set of vertical bars show the positions of the reflections for each space group model as indicated in the figure. The red line shows the calculated diffraction pattern based on the model used while the blue line at the bottom shows the difference between the observed data and the model. The peak splitting at ~ 14, 16 and 19.5°, amongst others, was used to determine the transition from hexagonal to monoclinic symmetry ($P6_3/mmc \rightarrow C2/c$) as the temperature was decreased. The bottom set of vertical markers corresponds to silver impurity reflections.*

In an effort to further probe the phase transition from hexagonal to monoclinic a series of single crystal diffraction measurements were collected starting at 300K and cooling to 100 K in approximately 10 K steps. The crystal diffracted strongly from 300 to 200 K but below this temperature the quality of the data degraded markedly. Upon heating, the crystal returned to its former quality. Figure 16 shows a plot of the volume of a single crystal of $Ba_3NaIr_2O_9$ cooled from 300 to 100 K. Full refinements were performed at 300 and 230 K with all other measurements collected over a shorter space of time sufficient to obtain unit cell dimensions only. At both 300 and 230 K the structure was found to be $P6_3/mmc$. There are at least three sets of changes in the slope of the plot potentially indicative of second order phase transitions. The first change occurs at 260 K, however, the single crystal measurements at 300 and 230 K do not support a change in space group. Coupled with this is the lack of peak splitting in the 200 K powder diffraction pattern, Figure 15. The second set of changes of slope occurs at 190 K and the third at 160 K. Given the poorer quality of the crystal data at lower temperatures, reflected here by the increasing size of the estimated standard deviation in Figure 16, it seems more likely that the onset of the phase transition from $P6_3/mmc$ to $C2/c$ occurs around 190 K than 160 K but in the absence of good quality low temperature single crystal or powder diffraction data it is impossible to be certain. At 100 K there is clear evidence of peak splitting in the powder patterns showing that the transition must start somewhere between ~ 190 and 100 K. Given the apparent problems collecting good quality low temperature single crystal data suitable to categorically identify the space group synchrotron powder diffraction measurements would be useful to determine more accurately the onset temperature and breadth of the phase transition.

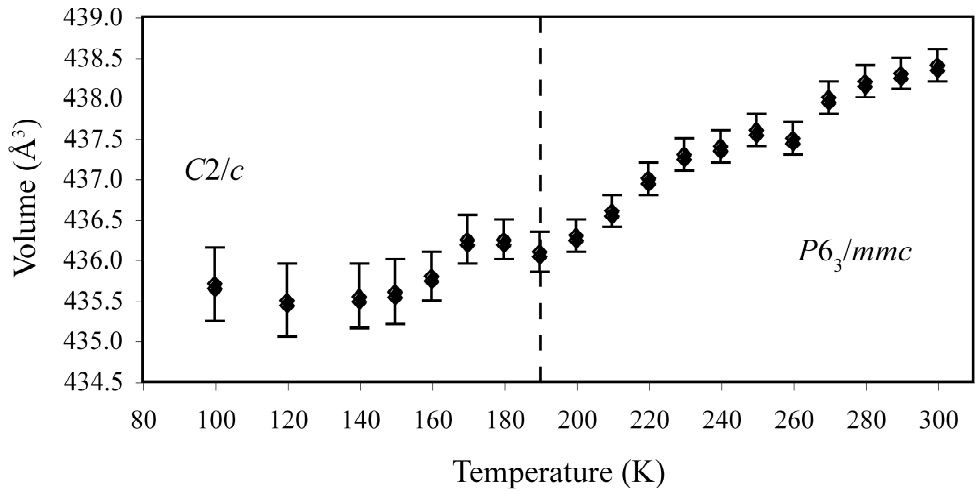

Figure 16: *Plot of volume change in the unit cell of a single crystal of $Ba_3NaIr_2O_9$ as a function of temperature. Values have been divided by 2 where appropriate to reference to an hexagonal unit cell for the sake of comparison. The dashed line indicates the onset of the $P6_3/mmc$ to $C2/c$ phase transition.*

Another possible phase scheme involves the transition from $P6_3/mmc$ to the orthorhombic space group *Cmcm* at 190 K and then to *C2/c* at 160 K. However, the transition from $P6_3/mmc$ to *Cmcm*, as exhibited in $Ba_3CoRu_2O_9$ and $Ba_3NaRu_2O_9$, must occur in a discontinuous fashion

since group theory arguments show that the transition cannot be second order and so is unlikely to occur in the case of $Ba_3NaIr_2O_9$. Additionally, single crystal lattice parameter measurements below 200 K show a general increase in the monoclinic beta splitting angle tending to rule out the possibility of an orthorhombic intermediate phase.

Figure 17 shows the high and low temperature structures of $Ba_3NaIr_2O_9$. At high temperature $Ba_3NaIr_2O_9$ is hexagonal ($P6_3/mmc$, No. 194). Moving along the *c* axis layers of face sharing Ir_2O_9 octahedra are corner linked with layers of single NaO_6 octahedra. Interspersed between these layers are Ba^{2+} ions in a 12-coordinate site. The low temperature $Ba_3NaIr_2O_9$ adopts a similar layered arrangement but in a monoclinic structure ($C2/c$, No. 15) with a doubling of the *b* axis such that $2a_{hex} \approx b_{mono}$.

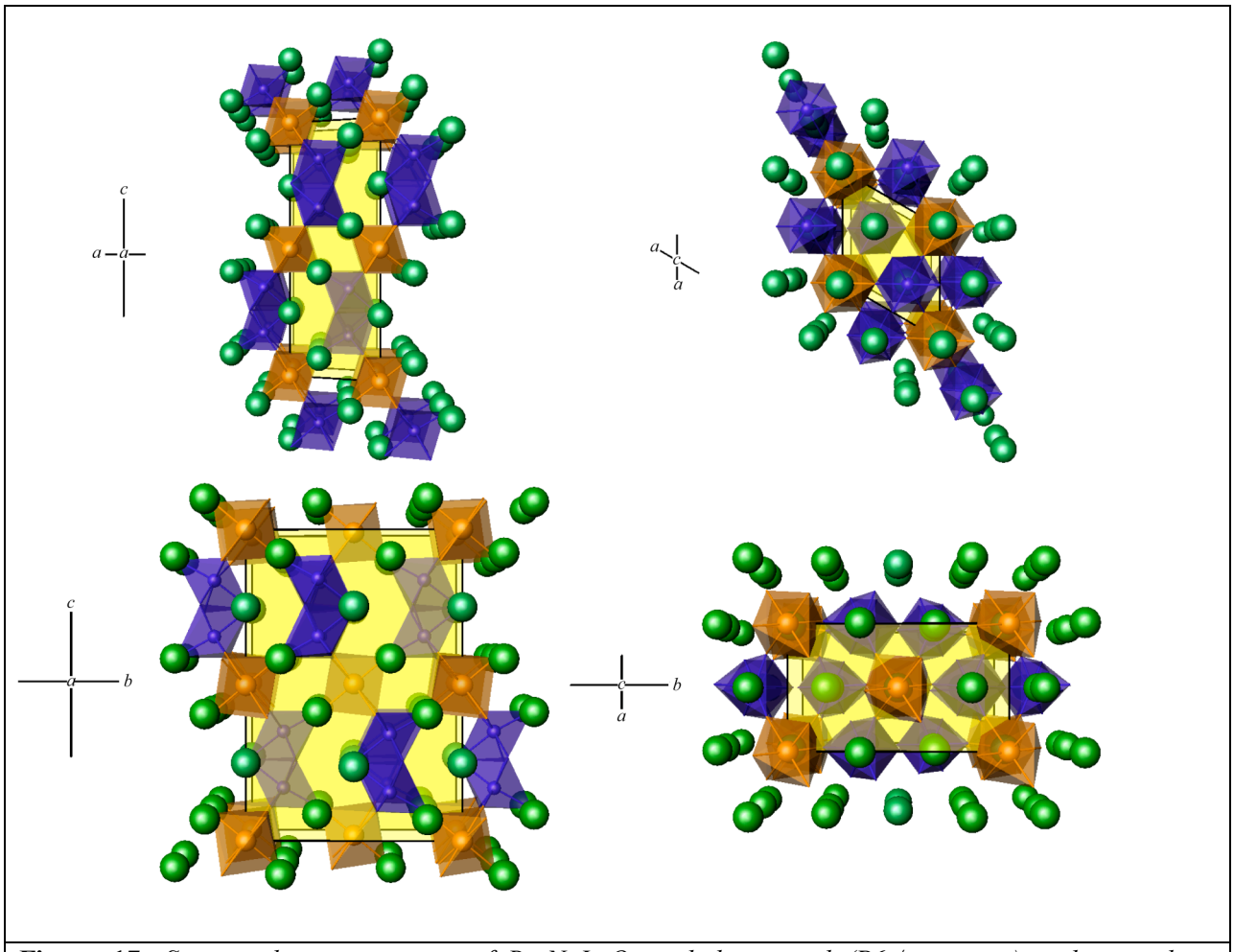

Figure 17: *Structural representation of $Ba_3NaIr_2O_9$ with hexagonal ($P6_3/mmc$, top) and monoclinic ($C2/c$, bottom) symmetry. The structures on the left show a view looking down the a axis while those on the right show the view looking down the c axis. The yellow prism shows the unit cell in each case. The blue polyhedra represent Ir_2O_9, the orange octahedra NaO_6 and the green spheres represent Ba^{2+} ions.*

Publications:

1. Mugavero III, S. J., Puzdrajkova, I. V., Smith, M. D., zur Loye, H.-C., " Sm_2NaIrO_6, a Monoclinically Distorted Double Perovskite", Acta Cryst., **2005**, *E61*, i3–i5.

2. Mugavero, S. J., Smith, M. D., zur Loye, H.-C., " The crystal growth and magnetic properties of Ln_2LiIrO_6 (Ln = Pr, Nd, Sm, Eu)", J. Solid State Chem., **2005**, *178*, 200-206.

3. zur Loye, H.-C., Smith, M. D., Lee, Y., Vogt, T., "High Pressure Investigation of Sr_3PbNiO_6", J. Alloys Comp., **2005**, *390*, 35-40.

4. Gemmill, W. R., Smith, M. D., Prozorov, R., zur Loye, H.-C., " Crystal Growth and Magnetic Properties of Lanthanide-Containing Osmium Double Perovskites, Ln_2NaOsO_6 (Ln = La, Pr, Nd)", Inorg. Chem., **2005**, *44*, 2639-2646.

5. Mugavero, S. J., Smith, M. D., zur Loye, H.-C., " $La_{2.50}K_{1.50}IrO_7$: An Example of an $n = 2$ Member of the $A_nB_{n-1}O_{3n}(A'_2O)$ Family of Perovskite Related Oxides", J. Solid State Chem., **2005**, *178*, 3176-3182.

6. Gemmill, W. R., Smith, M. D., Mozharivsky, Y. A., Miller, G. J., zur Loye, H.-C., " Crystal Growth, Structural Transitions and Magnetic Properties of the Fluorite-Related Osmates: Sm_3OsO_7, Eu_3OsO_7 and Gd_3OsO_7", Inorg. Chem., **2005**, *44*, 7047-7055.

7. Lufaso, M. W., zur Loye, H.-C., "Crystal Structures and Magnetic Properties of Mixed Iridium-Ruthenium Triple Perovskites: $Ba_3MRuIrO_9$ Part I: (M = Lanthanide, Y)", Inorg. Chem., **2005**, *44*, 9143-9153.

8. Lufaso, M. W., zur Loye, H.-C., " Crystal Structures and Magnetic Properties of Mixed Iridium-Ruthenium Triple Perovskites: $Ba_3MRuIrO_9$ Part II: (M = Li, Na, Mg, Ni, Zn, Bi, In)", Inorg. Chem., **2005**, *44*, 9154-9161.

9. Lufaso, M. W., Macquart, R. B., Lee, Y., Vogt, T., zur Loye, H.-C., "Pressure induced octahedral tilting distortion in Ba_2YTaO_6", Chem. Commun., **2006**, 168-170..

10. Mugavero, S. J., Smith, M. D., zur Loye, H.-C., "$La_9RbIr_4O_{24}$: A Rubidium-Containing Oxide with a New Structure Type", Inorg. Chem., **2006,** *45*, 946-948.

11. Macquart, R., Kim, S.-J., Gemmill, W. R., Stalick, J. K., Lee, Y., Vogt, T., zur Loye, H.-C., " Synthesis, Structure and Magnetic Properties of Sr_2NiOsO_6 and Ca_2NiOsO_6: Two New Osmium Containing Double Perovskites", Inorg. Chem., **2005**, *44*, 9676-9683.

12. Lufaso, M. W., Macquart, R. B., Lee, Y., Vogt, T., zur Loye, H.-C., "Pressure-Induced Phase Transition and Octahedral Tilt System Change of Ba_2BiSbO_6", J. Solid State Chem., **2006**, *179*, 917-922.

13. Macquart, R. B., Gemmill, W. R., Davis, M. J., Smith, M. D., zur Loye, H.-C., "Single Crystal Structure of the 2H-Related Perovskites ($A_{3-x}Na_x$)NaBO_6 (A = La, Pr, Nd; B = Rh, Pt)", Inorg. Chem., **2006**, *45*, 4391-4395.

14. Gemmill, W. R., Smith, M. D., zur Loye, H.-C., " Synthesis, Structural Characterization, and Magnetic Properties of the Antiferromagnetic Double Perovskites Ln_2LiOsO_6 (Ln = La, Pr, Nd, Sm)", J. Solid State Chem., **2006**, *179*, 1750-1756.

15. Macquart, R. B., Smith, M. D., zur Loye, H.-C., "Crystal Growth and Single Crystal Structures of RERhO_3 (RE = La, Pr, Nd, Sm, Eu, Tb) Orthorhodites from a K_2CO_3 Flux" Cryst. Growth Design, **2006**, *6*, 1361-1365.

16. Lufaso, M. W., zur Loye, H.-C., "Continuous Phase Transition in $Ba_3BiRuIrO_9$", Solid State Sciences, **2006**, *8*, 1051-1055.

17. Lufaso, M. W., Macquart, R. B., Lee, Y., Vogt, T., zur Loye, H.-C., "Structural Studies of Sr_2GaSbO_6, Sr_2NiMoO_6, and Sr_2FeNbO_6 Using Pressure and Temperature", J. Phys.: Cond. Mater., **2006**, *18*, 8761-8780.

18. Mugavero III, S. J., Smith, M. D., zur Loye, H.-C., " Hydroxide Flux Synthesis and Crystal Structure of the Ordered Palladate, $LuNaPd_6O_8$", J. Solid State Chem., **2006**, *179*, 3586-3589.

19. Lufaso, M. W., Gemmill, W. R., Mugavero III, S. J., Lee, Y., Vogt, T., zur Loye, H.-C., "Compression Mechanisms of Symmetric and Jahn-Teller Distorted Octahedra in Double Perovskites: A_2CuWO_6 (A = Sr, Ba), Sr_2CoMoO_6, and La_2LiRuO_6", J. Solid State Chem., **2006**, *179*, 3556-3561.

20. Puzdrjakova, I. V. Macquart, R.B.; Smith, M. D.; zur Loye, H.-C., "$Na_3Ca_2BiO_6$", Acta Cryst. E., **2007**, *E63*, 195-196.

21. Lufaso, M. W., Gemmill, W. R., Mugavero III, S. J., Lee, Y., Vogt, T., zur Loye, H.-C., "Pressure and Temperature Dependent X-ray Diffraction Studies of $NdCrO_3$" J. Alloys Comp., **2007**, *433*, 91-96.

22. Gemmill, W. R., Smith, M. D., zur Loye, H.-C., "$Ln_{14}Na_3Ru_6O_{36}$ (Ln = Pr, Nd): Two New Complex Lanthanide Containing Oxides of Ruthenium", Inorg. Chem., in press.

23. Mugavero, S. J., Smith, M. D., zur Loye, H.-C., "Crystal Growth and Structural Characterization of the New Ordered Palladates, LnKPdO_3 (Ln = La, Pr, Nd, Sm – Gd) and the Isostructural, partially Cu-Substituted Palladate, PrK($Cu_{0.14}Pd_{0.86}$)O_3", Inorg. Chem., in press.

24. Gemmill, W. R., Smith, M. D., zur Loye, H.-C., "Synthesis and Structural Characterization of Two New Hexagonal Osmates: $Ba_2Fe_{0.92}Os_{1.08}O_6$ and $Ba_2Co_{0.77}Os_{1.23}O_6$", Solid State Sciences, in press.